Science
AAAS

Strain-Induced Pseudo Magnetic Fields Greater Than 300 Tesla in Graphene Nanobubbles

N. Levy, *et al.*

Science **329**, 544 (2010);
DOI: 10.1126/science.1191700

($T_1 = 1/\gamma \sim \delta^2$ for $\delta \gg A_\perp^2$). Experimental data confirm this behavior (Fig. 3B). This dependence also explains why quantum jumps were not observed in previous experiments with NV centers performed at low magnetic fields [similar magnetic field–enabled decoupling of nuclear spin was proposed recently for alkaline earth metal ions (*10*, *22*)]. The dominance of flip-flop processes is also visible in the quantum state trajectory of the nuclear spin shown in Fig. 3C (top). Here, jumps obey the selection rule $\Delta m_I = \pm 1$ imposed by the flip-flop term H_A. From analyzing the whole quantum state trajectory, a matrix showing the transition probabilities can be obtained (Fig. 3C, bottom).

Single-shot measurement of a single nuclear spin places diamond among leading quantum computer technologies. The high readout fidelity (92%) demonstrated in this work is already close to the threshold for enabling error correction (*23*), although the experiments were carried out in a moderate-strength magnetic field. Even though the optical excitation induces complex dynamics in the NV center (including passage into singlet electronic state), the nuclear spin relaxation rates are defined solely by electron-nuclear flip-flop processes induced by hyperfine interaction. Therefore, we expect improvement of T_1 by two orders of magnitude (reaching seconds under illumination) when a magnetic field of 5 T is used. This will potentially allow readout fidelities comparable with that achieved for single ions in traps (*24*). The present technique can be applied to multiqubit quantum registers (*5*, *6*, *25*), enabling tests of nonclassical correlations. Finally, single-shot measurements open new perspectives for solid-state sensing technologies. Spins in diamond are considered to be among the promising candidates for nanoscale magnetic field sensing (*26*, *27*). Currently their performance is limited by photon shot noise (*26*): "Digital" QND will provide improvement over conventional photon counting in the case of short acquisition time. This requires that the electron spin state used for magnetic field sensing can be mapped onto the nuclear spin with high accuracy, but this was already shown to be practical in NV diamond (*5*).

References and Notes

1. N. A. Gershenfeld, I. L. Chuang, *Science* **275**, 350 (1997).
2. W. S. Warren, *Science* **277**, 1688 (1997).
3. T. D. Ladd *et al.*, *Nature* **464**, 45 (2010).
4. L. Childress *et al.*, *Science* **314**, 281 (2006).
5. M. V. G. Dutt *et al.*, *Science* **316**, 1312 (2007).
6. P. Neumann *et al.*, *Science* **320**, 1326 (2008).
7. G. D. Fuchs, V. V. Dobrovitski, D. M. Toyli, F. J. Heremans, D. D. Awschalom, *Science* **326**, 1520 (2009).
8. F. Jelezko, T. Gaebel, I. Popa, A. Gruber, J. Wrachtrup, *Phys. Rev. Lett.* **92**, 076401 (2004).
9. L. Jiang *et al.*, *Science* **326**, 267 (2009).
10. A. V. Gorshkov *et al.*, *Phys. Rev. Lett.* **102**, 110503 (2009).
11. The presented single-shot readout works in the same way and shows a similar fidelity for the nuclear spin of the ^{15}N isotope.
12. A. Batalov *et al.*, *Phys. Rev. Lett.* **100**, 077401 (2008).
13. Supporting material is available on *Science* Online.
14. T. M. Babinec *et al.*, *Nat. Nanotechnol.* **5**, 195 (2010).
15. V. B. Braginsky, F. Y. Khalili, *Rev. Mod. Phys.* **68**, 1 (1996).
16. N. Imoto, H. A. Haus, Y. Yamamoto, *Phys. Rev. A* **32**, 2287 (1985).
17. C. M. Caves, K. S. Thorne, R. W. P. Drever, V. D. Sandberg, M. Zimmermann, *Rev. Mod. Phys.* **52**, 341 (1980).
18. T. C. Ralph, S. D. Bartlett, J. L. O'Brien, G. J. Pryde, H. M. Wiseman, *Phys. Rev. A* **73**, 012113 (2006).
19. G. D. Fuchs *et al.*, *Phys. Rev. Lett.* **101**, 117601 (2008).
20. M. Steiner, P. Neumann, J. Beck, F. Jelezko, J. Wrachtrup, *Phys. Rev. B* **81**, 035205 (2010).
21. V. Jacques *et al.*, *Phys. Rev. Lett.* **102**, 057403 (2009).
22. I. Reichenbach, I. H. Deutsch, *Phys. Rev. Lett.* **99**, 123001 (2007).
23. E. Knill, *Nature* **434**, 39 (2005).
24. A. H. Myerson *et al.*, *Phys. Rev. Lett.* **100**, 200502 (2008).
25. L. Jiang, J. M. Taylor, A. S. Sorensen, M. D. Lukin, *Phys. Rev. A* **76**, 062323 (2007).
26. J. R. Maze *et al.*, *Nature* **455**, 644 (2008).
27. G. Balasubramanian *et al.*, *Nature* **455**, 648 (2008).

28. We thank F. Dolde for fabrication of microwave structures; N. Zarrabi for assistance with data analysis; J. Mayer and P. Bertet for helpful information on QND measurements in superconducting qubits; and M. D. Lukin, J. Twamley, F. Y. Khalili, and J. O'Brien for comments and discussions. We thank G. Denninger for the loan of a X-band microwave synthesizer. This work was supported by the European Union, Deutsche Forschungsgemeinschaft (SFB/TR21 and FOR1482), Bundesministerium für Bildung und Forschung, and Landesstiftung BW.

Supporting Online Material

www.sciencemag.org/cgi/content/full/science.1189075/DC1
Methods
SOM Text
Figs. S1 to S6
References

3 March 2010; accepted 21 June 2010
Published online 1 July 2010;
10.1126/science.1189075
Include this information when citing this paper.

Strain-Induced Pseudo–Magnetic Fields Greater Than 300 Tesla in Graphene Nanobubbles

N. Levy,[1,2]*† S. A. Burke,[1]*‡ K. L. Meaker,[1] M. Panlasigui,[1] A. Zettl,[1,2] F. Guinea,[3] A. H. Castro Neto,[4] M. F. Crommie[1,2]§

Recent theoretical proposals suggest that strain can be used to engineer graphene electronic states through the creation of a pseudo–magnetic field. This effect is unique to graphene because of its massless Dirac fermion-like band structure and particular lattice symmetry (C_{3v}). Here, we present experimental spectroscopic measurements by scanning tunneling microscopy of highly strained nanobubbles that form when graphene is grown on a platinum (111) surface. The nanobubbles exhibit Landau levels that form in the presence of strain-induced pseudo–magnetic fields greater than 300 tesla. This demonstration of enormous pseudo–magnetic fields opens the door to both the study of charge carriers in previously inaccessible high magnetic field regimes and deliberate mechanical control over electronic structure in graphene or so-called "strain engineering."

Graphene, a single atomic layer of carbon, displays remarkable electronic and mechanical properties (*1*, *2*). Many of graphene's distinctive properties arise from a linear band dispersion at low carrier energies (*3*) that leads to Dirac-like behavior within the two-dimensional (2D) honeycomb lattice—charge carriers travel as if their effective mass is zero (*1*). An intriguing recent prediction is that a distortion of the graphene lattice should create large, nearly uniform pseudo–magnetic fields and give rise to a pseudo–quantum Hall effect (*4*). Whereas an elastic strain can be expected to induce a shift in the Dirac point energy from local changes in electron density, it is also predicted to induce an effective vector potential that arises from changes in the electron-hopping amplitude between carbon atoms (*5*). This strain-induced gauge field can give rise to large pseudo–magnetic fields (B_s) for appropriately selected geometries of the applied strain (*1*, *6*). In such situations, the charge carriers in graphene are expected to circulate as if under the influence of an applied out-of-plane magnetic field (*7*–*10*). It has recently been proposed that a modest strain field with triangular symmetry will give approximately uniform, quantizing B_s upward of tens of tesla (*4*).

Here, we report the measurement of Landau levels (LLs) arising from giant strain-induced pseudo–magnetic fields in highly strained graphene nanobubbles grown on the Pt(111) surface. Lan-

[1]Department of Physics, University of California Berkeley, Berkeley, CA 94720, USA. [2]Materials Science Division, Lawrence Berkeley National Laboratory, Berkeley, CA 94720, USA. [3]Instituto de Ciencia de Materiales de Madrid (CSIC), Madrid 28049, Spain. [4]Department of Physics, Boston University, Boston, MA 02215, USA.

*These authors contributed equally to this work.
†Present address: Center for Nanoscale Science and Technology, National Institute of Standards and Technology, Gaithersburg, MD 20899, USA.
‡Present address: Department of Physics and Astronomy and Department of Chemistry, University of British Columbia, Vancouver, BC V6T 121, Canada.
§To whom correspondence should be addressed. E-mail: crommie@berkeley.edu

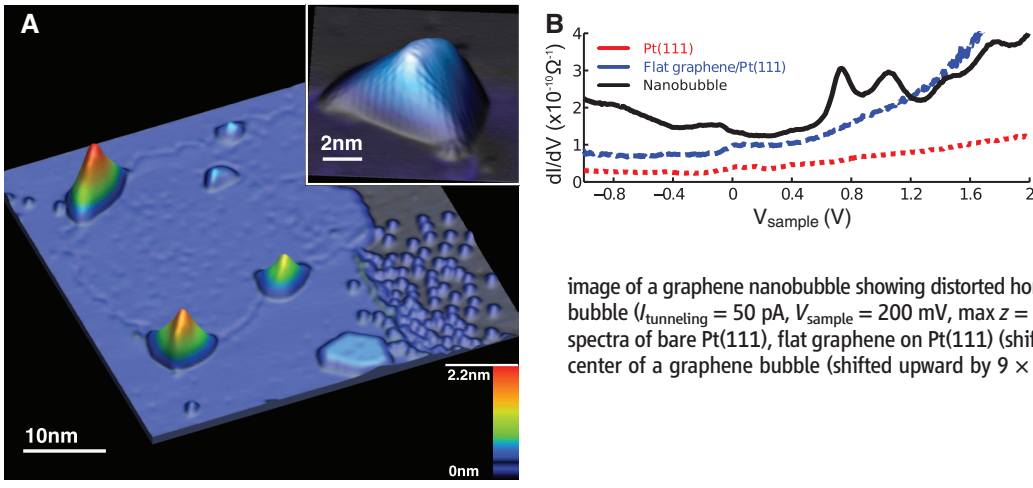

Fig. 1. STM images and STS spectra taken at 7.5 K. (**A**) Graphene monolayer patch on Pt(111) with four nanobubbles at the graphene-Pt border and one in the patch interior. Unreacted ethylene molecules and a small hexagonal graphene patch can be seen in the lower right ($I_{tunneling}$ = 50 pA, V_{sample} = 350 mV, 3D z-scale enhanced 4.6×). (Inset) High-resolution image of a graphene nanobubble showing distorted honeycomb lattice resulting from strain in the bubble ($I_{tunneling}$ = 50 pA, V_{sample} = 200 mV, max z = 1.6 nm, 3D z-scale enhanced 2×). (**B**) STS spectra of bare Pt(111), flat graphene on Pt(111) (shifted upward by 3×10^{-11} ohm^{-1}), and the center of a graphene bubble (shifted upward by 9×10^{-11} ohm^{-1}). V_{mod} = 20 mV.

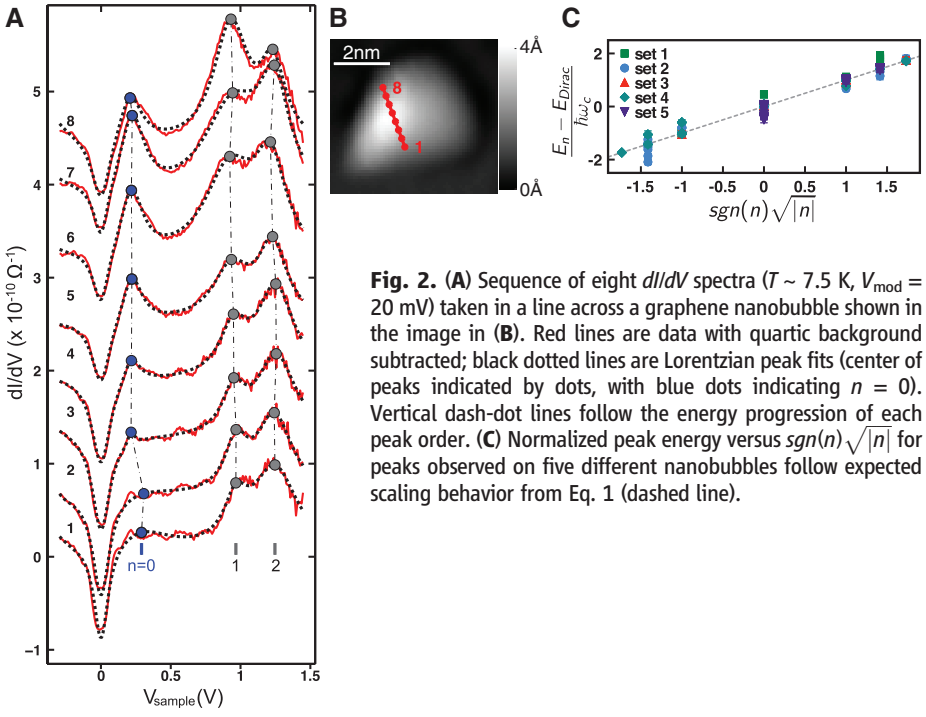

Fig. 2. (**A**) Sequence of eight *dI*/*dV* spectra (T ~ 7.5 K, V_{mod} = 20 mV) taken in a line across a graphene nanobubble shown in the image in (**B**). Red lines are data with quartic background subtracted; black dotted lines are Lorentzian peak fits (center of peaks indicated by dots, with blue dots indicating n = 0). Vertical dash-dot lines follow the energy progression of each peak order. (**C**) Normalized peak energy versus $sgn(n)\sqrt{|n|}$ for peaks observed on five different nanobubbles follow expected scaling behavior from Eq. 1 (dashed line).

dau quantization of the electronic spectrum was observed by scanning tunneling microscopy (STM), which revealed pseudo–magnetic fields in excess of 300 T. Such enormous strain-induced pseudo–magnetic fields may allow the electronic properties of graphene to be controlled through various schemes for applying strain (*11*), as well as the exploration of new high-field physical regimes.

Strained graphene nanobubbles were created by in situ growth of sub-monolayer graphene films in ultrahigh vacuum on a clean Pt(111) surface (*12*) in order to avoid external contamination and trapped gases. The epitaxial graphene was grown by exposure of Pt(111) to ethylene followed by annealing (*13*, *14*). Graphene grown on Pt is expected to be minimally coupled to the substrate, compared to graphene grown on other catalytic metals (*15*, *16*). A Dirac-like band structure is preserved for graphene on Pt(111), as verified by a recent photoemission study (*17*). An STM topograph of the graphene/Pt(111) surface prepared in this manner (Fig. 1A) reveals a flat graphene patch (partially surrounded by Pt) that encompasses five graphene nanobubbles. Graphene nanobubbles frequently appear near the edges of a graphene patch, but are also sometimes observed in the center of flat patches or near the boundaries between patches and are presumably pinned near these locations (Fig. 1A). These nanobubbles are likely related to the larger-scale "wrinkle" structures observed by low energy electron microscopy that form upon cooling as a result of the differing thermal expansion coefficients of graphene and the platinum surface (*17*).

Individual nanobubbles often have a triangular shape (Fig. 1A, inset), reflecting the lattice symmetry of the graphene and the underlying Pt surface, and are typically 4 to 10 nm across and 0.3 to 2.0 nm tall. Atomic-resolution imaging of the nanobubbles confirms the honeycomb structure of graphene here (Fig. 1A, inset), although the lattice is distorted because of the large strain occurring in these structures. The expected strain-induced pseudo–magnetic field in a graphene nanobubble can be estimated by using the relation $\Phi = (\beta h^2/la)\Phi_0$ for the flux per ripple in a distorted graphene sheet (*6*), where h is the height, l is the width, a is on the order of the C-C bond length, and Φ_0 is the quantum of flux. The parameter $\beta = \partial\log(t)/\partial\log(a)$ relates the change in the hopping amplitude between nearest neighbor carbon atoms (t) to bond length and has a typical magnitude of $2 < \beta < 3$ for graphene. For a nanobubble of l = 4 nm and h = 0.5 nm, this yields a B_s of order 100 T. The large curvature and correspondingly high strain incorporated into the triangular nanoscale bubbles observed here make them ideal candidates for the observation of pseudo-LL because of large strain-induced pseudo–magnetic fields.

The local electronic structure of strained graphene nanobubbles and surrounding graphene films was characterized by scanning tunneling spectroscopy (STS) performed at ~ 7.5 K by using standard lock-in techniques to obtain differential conductance (*dI*/*dV*). The measurement of *dI*/*dV* reflects features in the local density of states (LDOS) of the surface at the position of the STM tip (*18*). STS measurement of the bare Pt surface was used to calibrate the LDOS of the tip upon approach and between sequences of spectra. STS spectra measured over the bare Pt regions (Fig. 1B) are relatively featureless and show the expected Pt(111) surface state (*19*). Spectra recorded over the flat graphene patches show a subtly modified structure compared with the clean Pt(111) surface, and no clear signatures of the graphene Dirac point were observed in these regions (Fig. 1B). Spectra measured at the boundary between the flat graphene and the nanobubbles (fig. S2) exhibit features consistent with a Dirac point located ~300 mV above the Fermi energy, as recently observed by photoemission (*17*), as well as a gaplike feature with a full width at half maximum (FWHM) of 127 ± 9 mV centered at the Fermi energy (V_{sample} = 0) recently

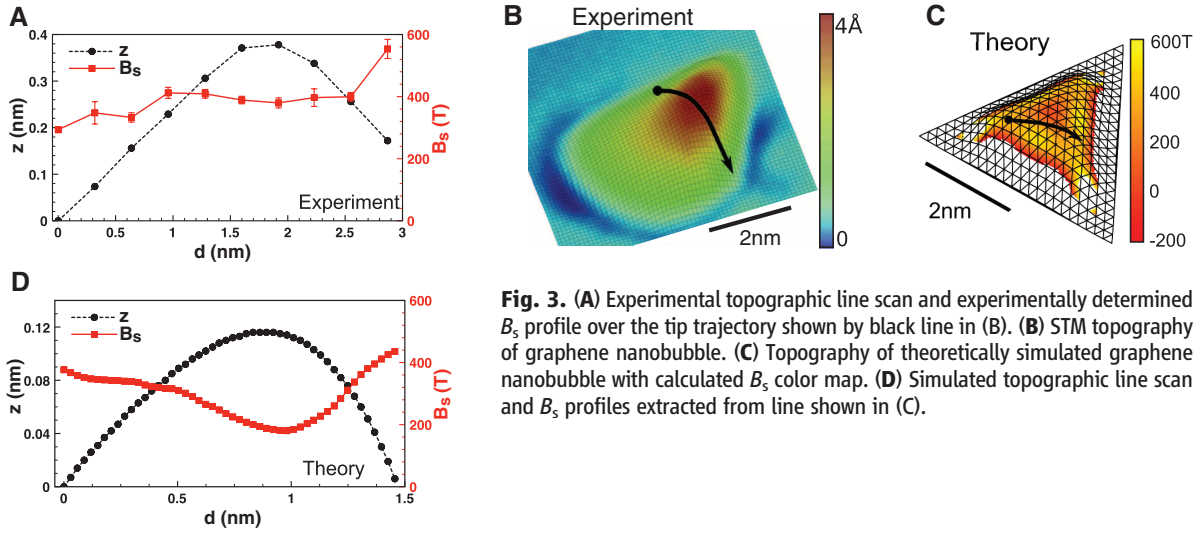

Fig. 3. (**A**) Experimental topographic line scan and experimentally determined B_s profile over the tip trajectory shown by black line in (B). (**B**) STM topography of graphene nanobubble. (**C**) Topography of theoretically simulated graphene nanobubble with calculated B_s color map. (**D**) Simulated topographic line scan and B_s profiles extracted from line shown in (C).

associated with phonon-assisted inelastic tunneling (*20*).

STS measurements made directly over the nanobubble regions exhibit a succession of relatively strong peaks, spaced by more than 100 meV, which do not appear in the spectra on other regions of the sample (Fig. 1B). The peaks are typically weaker at negative bias, which may be attributed to the expected shorter vertical extension of wavefunctions at lower energies. These peaks in the LDOS of the graphene nanobubble are unlike features seen previously in STS performed on graphene in the absence of a magnetic field on SiC (*21*, *22*) and SiO_2 (*20*, *23*) substrates and often overwhelm the usual graphene features. Figure 2A shows a series of spectra taken at different positions across a single nanobubble (topography shown in Fig. 2B). These spectra display the typical nanobubble peak structure as well as the inelastic feature at the Fermi energy described above [a broader bias range is shown in (fig. S3)]. Similar peak structure was observed on 10 different nanobubbles with four different STM tips, with some variation in peak spacing and amplitude that we presume was caused by variations in strain-induced electronic structure arising from different nanobubble geometries.

These peaks observed in the nanobubble LDOS can be attributed to LLs originating from a strain-induced pseudo–magnetic field. Other possible origins that we rule out as unlikely include confinement effects and defect creation. Confinement of Dirac fermions in graphene is difficult because of Klein tunnelling and the suppression of backscattering (*1*). If confinement somehow occurred at the nanobubble edges, the peaks observed would be expected to follow a different progression, most notably missing the $n = 0$ peak observed in spectra taken at the center of most nanobubbles (*24*). Confinement would also result in strong nodal patterns in LDOS (*24*), which were not observed. The production of defect states by strain is also unlikely because of the high energetic barrier toward defect creation. It is possible that some nanobubbles were formed at defect sites in the as-grown graphene, but the nanobubbles that we measured did not show signatures of defect physics in spectroscopy, such as tip height dependence of peak positions associated with the charging of defect states.

The most likely explanation for the nanobubble peaks is that they arise from a large, relatively uniform strain-induced pseudo–magnetic field. This pseudo–magnetic field is expected to mimic the influence of a real magnetic field applied perpendicular to the graphene sheet and give rise to LLs (*4*). These appear as a series of peaks in STS as they do for the case of a real magnetic field (*25*, *26*). Specifically, the 2D massless Dirac nature of charge carriers near the Fermi energy causes the progression of peaks in the LDOS to follow the expression (*7*, *8*):

$$E_n = \mathrm{sgn}(n)\hbar\omega_c\sqrt{|n|} + E_{\mathrm{Dirac}},$$

$$\omega_c = \sqrt{2e\hbar v_F^2 B_s} \qquad (1)$$

where E_n is the position in energy of the nth LL with respect to the Fermi level, ω_c is the cyclotron resonance frequency arising from B_s, and v_F is the Fermi velocity. Both positive and negative n will appear symmetrically about the Dirac point, corresponding to electron and hole states, respectively, as well as an $n = 0$ state coincident with the Dirac point (*1*, *7*, *8*).

The energy progression expected for LLs in graphene can be compared to STS data taken on a nanobubble by fitting the spectra with a sequence of Lorentzian peaks following Eq. 1 with a simple polynomial background (Fig. 2A). The observed peak structure follows the expected progression well, and a value of B_s for position "1" in Fig. 2A was determined to be 350 ± 40 T (energies of the $n = 0$, 1, and 2 states from the fit are shown below the spectrum for this position). Additional peaks that largely follow the expected $\mathrm{sgn}(n)\sqrt{|n|}$ progression were also observed over a wider bias range. Small deviations from this progression occur for higher energy peaks, because the graphene dispersion is not strictly linear in this range. A plot of normalized energy $(E_n - E_{\mathrm{Dirac}})/\hbar\omega_c$ versus $\mathrm{sgn}(n)\sqrt{|n|}$, shown in Fig. 2C, compiled from spectra on five different nanobubbles, demonstrates the expected scaling behavior for LLs in graphene.

The offset and spacing of the peak progression changes over different positions on individual nanobubbles, indicating a spatial variation of B_s and E_{Dirac}. The B_s profile across a strained nanobubble was extracted from the spectral peak spacing at different positions across a nanobubble, shown in Fig. 3B. As seen in Fig. 3A, the B_s profile is reasonably flat across the center of the bubble, indicating a relatively uniform pseudo–magnetic field of 300 to 400 T for this particular geometry. E_{Dirac}, coincident with the $n = 0$ LL, ranges from 0.2 to 0.3 eV across this region of the nanobubble. This variation in E_{Dirac} indicates scalar potential variations across the nanobubble, as expected for an elastic deformation that does not constitute a pure shear strain (*1*, *5*).

To compare the experimental spatial dependence of the strain-induced pseudo–magnetic field to theoretical predictions, we simulated a triangular nanobubble with similar geometry to that shown in Figs. 2A and 3B by using continuum elasticity theory (*27*) [see supporting information for details (*12*)]. In this calculation, the edges of a triangular graphene patch were brought in toward the center to simulate the strain arising from the different coefficients of thermal expansion of graphene and the underlying Pt(111) substrate during experimental sample preparation. The predicted pseudo–magnetic field arising from this strain field was also calculated following (*4*). A 3D plot of the simulated nanobubble shape with the pseudo–magnetic field strength shown as a color map is displayed in Fig. 3C (the corresponding experimental nanobubble is shown in Fig. 3B). The simulated and experimental topographic profiles agree well, as seen by the com-

parison between Fig. 3, A and D. The simulated B_s profile (Fig. 3D) also agrees reasonably well with the experimentally extracted B_s (Fig. 3A) given that there are some differences in shape and uncertainty in the exact boundary conditions. The main discrepancy is that the experimental B_s profile appears much more uniform than the simulated one, which may be attributed to spatial averaging of the LDOS over the magnetic length scale of ~1.5 nm. The simulated and experimental nanobubbles both exhibit a relatively uniform strain-induced pseudo–magnetic field of 200 to 400 T across the central region with increasing field at the edges.

The exceptional flexibility and strength of graphene membranes (*28*, *29*) coupled with the large strain-induced fields observed suggest that strain engineering of nanoscale energy levels (*11*, *30*) may be a viable means of controlling the electronic structure of graphene, even at room temperature. The experimental demonstration of these enormous pseudo–magnetic fields also provides a new basis for the study of extreme high magnetic field regimes in a condensed-matter environment.

References and Notes

1. A. H. Castro Neto, F. Guinea, N. M. R. Peres, K. S. Novoselov, A. K. Geim, *Rev. Mod. Phys.* **81**, 109 (2009).
2. A. K. Geim, K. S. Novoselov, *Nat. Mater.* **6**, 183 (2007).
3. P. R. Wallace, *Phys. Rev.* **71**, 622 (1947).
4. F. Guinea, M. I. Katsnelson, A. K. Geim, *Nat. Phys.* **6**, 30 (2010).
5. F. Guinea, A. K. Geim, M. I. Katsnelson, K. S. Novoselov, *Phys. Rev. B* **81**, 035408 (2010).
6. F. Guinea, M. I. Katsnelson, M. A. H. Vozmediano, *Phys. Rev. B* **77**, 075422 (2008).
7. Y. B. Zhang, Y. W. Tan, H. L. Stormer, P. Kim, *Nature* **438**, 201 (2005).
8. K. S. Novoselov *et al.*, *Nature* **438**, 197 (2005).
9. K. I. Bolotin, F. Ghahari, M. D. Shulman, H. L. Stormer, P. Kim, *Nature* **462**, 196 (2009).
10. X. Du, I. Skachko, F. Duerr, A. Luican, E. Y. Andrei, *Nature* **462**, 192 (2009).
11. V. M. Pereira, A. H. Castro Neto, *Phys. Rev. Lett.* **103**, 046801 (2009).
12. Materials and methods are available as supporting material on *Science* Online.
13. T. A. Land, T. Michely, R. J. Behm, J. C. Hemminger, G. Comsa, *Surf. Sci.* **264**, 261 (1992).
14. M. Enachescu, D. Schleef, D. F. Ogletree, M. Salmeron, *Phys. Rev. B* **60**, 16913 (1999).
15. A. B. Preobrajenski, M. L. Ng, A. S. Vinogradov, N. Martensson, *Phys. Rev. B* **78**, 073401 (2008).
16. M. Gao *et al.*, *Appl. Phys. Lett.* **96**, 053109 (2010).
17. P. Sutter, J. T. Sadowski, E. Sutter, *Phys. Rev. B* **80**, 245411 (2009).
18. J. A. Stroscio, W. J. Kaiser, *Scanning Tunneling Microscopy* (Academic Press, San Diego, CA, 1993).
19. J. Wiebe *et al.*, *Phys. Rev. B* **72**, 193406 (2005).
20. Y. B. Zhang *et al.*, *Nat. Phys.* **4**, 627 (2008).
21. V. W. Brar *et al.*, *Appl. Phys. Lett.* **91**, 122102 (2007).
22. G. M. Rutter *et al.*, *Science* **317**, 219 (2007).
23. V. W. Brar *et al.*, *Phys. Rev. Lett.* **104**, 036805 (2010).
24. J. Akola, H. P. Heiskanen, M. Manninen, *Phys. Rev. B* **77**, 193410 (2008).
25. D. L. Miller *et al.*, *Science* **324**, 924 (2009).
26. G. Li, E. Y. Andrei, *Nat. Phys.* **3**, 623 (2007).
27. H. S. Seung, D. R. Nelson, *Phys. Rev. A* **38**, 1005 (1988).
28. C. Lee, X. D. Wei, J. W. Kysar, J. Hone, *Science* **321**, 385 (2008).
29. J. S. Bunch *et al.*, *Nano Lett.* **8**, 2458 (2008).
30. W. Z. Bao *et al.*, *Nat. Nanotechnol.* **4**, 562 (2009).

31. Research supported by the Director, Office of Science, Office of Basic Energy Sciences, Materials Sciences and Engineering Division, of the U.S. Department of Energy (DOE) under contract no. DE-AC02-05CH11231 (instrumentation development and materials synthesis) and DOE contract no. DE-FG02-08ER46512 (experimental data analysis), by the Office of Naval Research Multidisciplinary University Research Initiative (MURI) award no. N00014-09-1-1066 (experimental STM measurements) and MURI award no. N00014-09-1-1063 (electronic structure calculations), and by Ministerio de Ciencia e Innovación (MICINN) (Spain), award nos. FIS2008-00124/CSD2007-00010 (continuum elasticity simulations). A.H.C.N. acknowledges the support of the Miller Institute for Basic Research. S.A.B. and K.L.M. acknowledge fellowship support from Natural Sciences and Engineering Research Council (Canada) and NSF, respectively. The authors declare no competing financial interests. Requests for materials should be addressed to M.F.C.

Supporting Online Material

www.sciencemag.org/cgi/content/full/329/5991/544/DC1
Materials and Methods
SOM Text
Figs. S1 to S7
References

30 April 2010; accepted 29 June 2010
10.1126/science.1191700

Probing the Superfluid–to–Mott Insulator Transition at the Single-Atom Level

W. S. Bakr,[1] A. Peng,[1] M. E. Tai,[1] R. Ma,[1] J. Simon,[1] J. I. Gillen,[1] S. Fölling,[1,2] L. Pollet,[1] M. Greiner[1]*

Quantum gases in optical lattices offer an opportunity to experimentally realize and explore condensed matter models in a clean, tunable system. We used single atom–single lattice site imaging to investigate the Bose-Hubbard model on a microscopic level. Our technique enables space- and time-resolved characterization of the number statistics across the superfluid–Mott insulator quantum phase transition. Site-resolved probing of fluctuations provides us with a sensitive local thermometer, allows us to identify microscopic heterostructures of low-entropy Mott domains, and enables us to measure local quantum dynamics, revealing surprisingly fast transition time scales. Our results may serve as a benchmark for theoretical studies of quantum dynamics, and may guide the engineering of low-entropy phases in a lattice.

Microscopic measurements can reveal properties of complex systems that are not accessible through statistical ensemble measurements. For example, scanning tunneling microscopy has allowed physicists to identify the importance of nanoscale spatial inhomogeneities in high-temperature superconductivity (*1*), and single-molecule microscopy (*2*) has enabled studies of local dynamics in chemical reactions, revealing the importance of multiple reaction pathways (*3*). Whereas previous ultracold quantum gas experiments focused primarily on statistical ensemble measurements, the recently introduced single atom–single lattice site imaging technique in a quantum gas microscope (*4*) opens the door for probing and controlling quantum gases on a microscopic level. Here, we present a microscopic study of an atom-lattice system that realizes the bosonic Hubbard model and exhibits a quantum phase transition from a superfluid to a Mott insulator (*5*–*7*).

In the weakly interacting superfluid regime, the many-body wave function factorizes into a product of states with well-defined phase on each lattice site, known as coherent states, with Poissonian number fluctuations. As the strength of the interaction increases, the number distribution is narrowed, resulting in a fixed atom number state on each site deep in the Mott insulator regime. We study this change in the number statistics across the transition; these microscopic studies are complementary to previous experiments that have focused on measuring ensemble properties such as long-range phase coherence, excitation spectra, or compressibility (*7*–*9*). Local properties such as on-site number statistics (*10*) had been accessible only indirectly (*8*, *11*, *12*) and were averaged over several shells of superfluid and Mott insulating domains in the inhomogeneous system, complicating quantitative interpretation. More recently, the shell structure was imaged through tomographic (*13*), spectroscopic (*14*), and in situ imaging techniques, coarse-grained over several lattice sites (*15*).

We started with a two-dimensional (2D) ^{87}Rb Bose-Einstein condensate of a few thousand atoms confined in a single well of a standing wave, with a harmonic oscillator length of 130 nm (*16*). The condensate resided 9 μm from an in-vacuum lens that was part of an imaging system with a resolution of ~600 nm. This high-resolution system

[1]Department of Physics, Harvard University, Cambridge, MA 02138, USA. [2]Institut für Physik, Ludwig-Maximilians-Universität, 80799 München, Germany.

*To whom correspondence should be addressed. E-mail: greiner@physics.harvard.edu